UNIVERSITY OF LEEDS

This is a repository copy of *Nanobody-aided crystallization of the transcription regulator PaaR2 from Escherichia coli O157:H7*.

White Rose Research Online URL for this paper:
https://eprints.whiterose.ac.uk/180323/

Version: Published Version

Article:
De Bruyn, P, Prolič-Kalinšek, M, Vandervelde, A et al. (7 more authors) (2021) Nanobody-aided crystallization of the transcription regulator PaaR2 from Escherichia coli O157:H7. Acta Crystallographica Section F: Structural Biology Communications, 77 (10). pp. 374-384. ISSN 2053-230X

https://doi.org/10.1107/s2053230x21009006

Reuse
Items deposited in White Rose Research Online are protected by copyright, with all rights reserved unless indicated otherwise. They may be downloaded and/or printed for private study, or other acts as permitted by national copyright laws. The publisher or other rights holders may allow further reproduction and re-use of the full text version. This is indicated by the licence information on the White Rose Research Online record for the item.

Takedown
If you consider content in White Rose Research Online to be in breach of UK law, please notify us by emailing eprints@whiterose.ac.uk including the URL of the record and the reason for the withdrawal request.

White Rose university consortium
Universities of Leeds, Sheffield & York

eprints@whiterose.ac.uk
https://eprints.whiterose.ac.uk/

Check for updates

STRUCTURAL BIOLOGY COMMUNICATIONS

ISSN 2053-230X

Nanobody-aided crystallization of the transcription regulator PaaR2 from *Escherichia coli* O157:H7

Pieter De Bruyn,[a,b]‡ Maruša Prolič-Kalinšek,[a,b]‡ Alexandra Vandervelde,[a,b] Milan Malfait,[a] Yann G.-J. Sterckx,[a,b,c] Frank Sobott,[d,e] San Hadži,[f] Els Pardon,[a,b] Jan Steyaert[a,b] and Remy Loris[a,b]*

[a]Structural Biology Brussels, Vrije Universiteit Brussel, Pleinlaan 2, 1050 Brussels, Belgium, [b]Center for Structural Biology, VIB, Pleinlaan 2, 1050 Brussels, Belgium, [c]Laboratory of Medical Biochemistry (LMB) and the Infla-Med Centre of Excellence, University of Antwerp, Universiteitsplein 1, 2610 Wilrijk, Belgium, [d]Astbury Centre for Structural Molecular Biology, University of Leeds, Leeds LS2 9JT, United Kingdom, [e]School of Molecular and Cellular Biology, University of Leeds, Leeds LS2 9JT, United Kingdom, and [f]Department of Physical Chemistry, Faculty of Chemistry and Chemical Technology, University of Ljubljana, Večna pot 113, 1000 Ljubljana, Slovenia. *Correspondence e-mail: remy.loris@vub.be

Received 1 August 2021
Accepted 30 August 2021

Edited by R. L. Stanfield, The Scripps Research Institute, USA

‡ PDB and MP-K contributed equally to this work and should be considered joint first authors.

Keywords: toxin–antitoxin modules; transcription regulation; macromolecular complexes; nanobody-aided crystallization; crystallization chaperones; *Escherichia coli* O157:H7; PaaR2.

Supporting information: this article has supporting information at journals.iucr.org/f

paaR2–paaA2–parE2 is a three-component toxin–antitoxin module found in prophage CP-993P of *Escherichia coli* O157:H7. Transcription regulation of this module occurs via the 123-amino-acid regulator PaaR2, which forms a large oligomeric structure. Despite appearing to be well folded, PaaR2 withstands crystallization, as does its N-terminal DNA-binding domain. Native mass spectrometry was used to screen for nanobodies that form a unique complex and stabilize the octameric structure of PaaR2. One such nanobody, Nb33, allowed crystallization of the protein. The resulting crystals belong to space group *F*432, with unit-cell parameter a = 317 Å, diffract to 4.0 Å resolution and are likely to contain four PaaR2 monomers and four nanobody monomers in the asymmetric unit. Crystals of two truncates containing the N-terminal helix–turn–helix domain also interact with Nb33, and the corresponding co-crystals diffracted to 1.6 and 1.75 Å resolution.

1. Introduction

X-ray crystallography, as witnessed by the more than 120 000 entries in the Protein Data Bank (Berman *et al.*, 2000), remains one of the most important methods in structural biology. Advances in technology and methodology for data collection and structure determination allow more and more complex and large macromolecular assemblies to be tackled. While it is often assumed that any pure, stable and well folded protein can be crystallized, this step often remains the greatest bottleneck in modern X-ray structure determination (Holcomb *et al.*, 2017). A typical crystallographic study starts with overexpression and purification of the target molecule, followed by testing the protein using one or more commercial crystallization screens. In the case of success, the crystals are further optimized if necessary. In the case of failure, alternative purification protocols, expression strategies or constructs need to be designed.

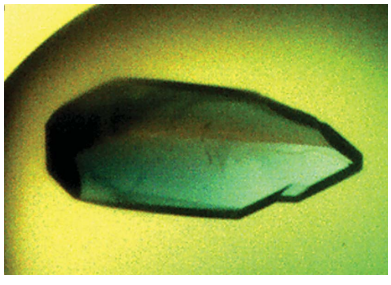

Several techniques have been developed to enhance success in crystallization and crystal optimization. These include the screening of additives, the modification of surface residues, either chemically (Goldschmidt *et al.*, 2014; Derewenda & Vekilov, 2006; Schubot & Waugh, 2004) or via site-specific mutagenesis (Ruggiero *et al.*, 2012; Roos *et al.*, 2006), (heterologous) seeding techniques and the removal of flexible regions through limited proteolysis (Tong *et al.*, 2014).

An interesting approach to tackle difficult targets is the use of crystallization chaperones: proteins that increase the crystallization probability of the target by binding to it with high affinity, thereby stabilizing its structure and/or conformation and hence providing a different surface that may be involved in crystal lattice interactions (Koide, 2009). Originally, antibody fragments such as Fab or Fv were used to facilitate the crystallization of membrane proteins (Hunte & Michel, 2002; Uysal *et al.*, 2009; Stahl *et al.*, 2014). Because of the inherent difficulties with the production of Fab and Fv fragments, several alternatives have been explored. So-called designed ankyrin-repeat proteins (DARPins) have been documented to be useful crystallization chaperones (Sennhauser & Grütter, 2008). The wide diversity in unique structural features of antibodies (or fragments thereof) from various organisms has also provided the crystallographic community with useful tools (de Los Rios *et al.*, 2015).

So-called nanobodies (or VHH antibodies) are single-domain VH fragments from camelid heavy-chain-only antibodies (Hamers-Casterman *et al.*, 1993). In contrast to fragments from classic antibodies, nanobodies can be expressed with high yields and are very soluble (Muyldermans, 2001). They also show good thermodynamic stability (Dumoulin *et al.*, 2002) and are able to target epitopes that are difficult for classical antibodies, in particular deep clefts (Desmyter *et al.*, 1996). Nanobodies have been shown to be very suitable as crystallization chaperones. They can stabilize dynamic proteins and allow easier crystallization by masking flexible regions, as was first employed for the *Escherichia coli* antitoxin MazE (Loris *et al.*, 2003) and subsequently for other proteins with flexible regions (Koide, 2009; Korotkov *et al.*, 2009). Their high specificity also allows them to stabilize specific conformations in multi-domain proteins (Rasmussen, Choi *et al.*, 2011; Huang *et al.*, 2015) and to stabilize macromolecular complexes (Rasmussen, DeVree *et al.*, 2011; Baranova *et al.*, 2012).

PaaR2 is a 123-amino-acid transcription regulator encoded in the *paaR2–paaA2–parE2* operon that is present within prophage CP-993P in the genome of *E. coli* O157:H7 (Hallez *et al.*, 2010). It consists of a predicted helix–turn–helix (HTH) domain followed by a predicted coiled-coil domain (De Bruyn *et al.*, 2019), and a *BLAST* search revealed that the protein shows weak sequence similarity (14% sequence identity) to residues 14–135 of the C2 repressor of *Salmonella* bacteriophage P22. The other two proteins encoded in the operon, ParE2 and PaaA2, form a type II toxin–antitoxin module where the toxin ParE2 acts on an as yet unidentified target. The antitoxin PaaA2 is an intrinsically disordered protein (Sterckx *et al.*, 2014) that wraps around ParE2, resulting in the formation of a heterohexadecameric complex (Sterckx *et al.*, 2016). In typical toxin–antitoxin modules, the antitoxin and the toxin–antitoxin complex regulate the expression of the operon. However, PaaA2 does not possess a DNA-binding domain (Sterckx *et al.*, 2014) and transcription regulation of the operon requires PaaR2 (Hallez *et al.*, 2010; De Bruyn *et al.*, 2019). The molecular details of how PaaR2 interacts with its DNA target and whether this interaction is influenced by ParE2, PaaA2 or the ParE2–PaaA2 complex remain unclear. In this paper, we report the expression, purification and nanobody-assisted crystallization of PaaR2. The resulting structure is expected to contribute to our understanding of the regulation of the *paaR2–paaA2–parE2* toxin–antitoxin module.

2. Materials and methods

2.1. Cloning, expression and purification of PaaR2

The cloning and expression of full-length PaaR2 with a C-terminal His tag and a serine substituted for Cys120 has been described previously (De Bruyn *et al.*, 2019). The expression plasmid (pET15bR2HisC120SA2E2) not only contains the mutated *paaR2* gene, but also the coding sequences for PaaA2 and ParE2. Cloning and production details are summarized in Table 1. For protein production, pET15bR2HisC120SA2E2 was transformed into the expression strain *E. coli* BL21 (DE3).

A colony of *E. coli* BL21 (DE3) (pET15bR2HisC120SA2E2) was grown overnight at 37°C in 300 ml LB medium supplemented with ampicillin (100 µg ml^{-1}). The overnight culture was diluted 50 times in 12 1 l flasks of LB and grown at 37°C with shaking. When the OD_{600} reached 0.6–0.8, the cells were induced with 1 m*M* isopropyl β-D-1-thiogalactopyranoside (IPTG). After further incubation for 4 h at 37°C with shaking, the cells were pelleted for 13 min at 4°C using a JLA-8.1000 rotor at 5000 rev min^{-1} (6238*g*). Each pellet was resuspended in lysis buffer [20 m*M* Tris–HCl pH 7.3, 500 m*M* NaCl, 20 m*M* $MgCl_2$, 0.1 mg ml^{-1} 4-(2-aminoethyl)benzenesulfonyl fluoride hydrochloride (AEBSF), 1 µg ml^{-1} leupeptin, 50 µg ml^{-1} DNase I]. This suspension was then left to stir for 30 min at 4°C. Lysis was achieved by sonication three times for 1 min. The lysate was centrifuged for 45 min using a JA-20 rotor at 18 000 rev min^{-1} (39 191*g*) and was loaded onto a 5 ml HisTrap HP Ni^{2+}-Sepharose column (GE Healthcare) that had been pre-equilibrated with least one column volume of buffer *A* (20 m*M* Tris–HCl pH 7.3, 500 m*M* NaCl, 5 m*M* imidazole). After a wash period, buffer *B* (20 m*M* Tris–HCl pH 7.3, 500 m*M* NaCl, 1 *M* imidazole) was added to generate a linear gradient of 0–1 *M* imidazole over 50 column volumes. The fractions containing the protein of interest, PaaR2, were pooled and concentrated to a volume of 2 ml.

The Ni–NTA-purified protein was subsequently loaded onto a Superdex 200 16/90 SEC column (GE Healthcare) which had been washed and pre-equilibrated with at least one column volume of SEC buffer (20 m*M* Tris–HCl pH 7.3, 500 m*M* NaCl). The eluted samples were checked for purity by SDS–PAGE and the relevant fractions were pooled, flash-frozen and stored at −20°C.

2.2. Cloning, expression and purification of PaaR2$^{1-57}$ and PaaR2$^{1-66}$

The plasmid pET15b-PaaR2His-PaaA2-ParE2 was PCR-amplified, except for the C-terminal end sequence that was desired to be deleted, using overlapping primers and Q5

Table 1
Macromolecule-production information.

Construct	PaaR2HisC120S	PaaR2$^{1–57}$	PaaR2$^{1–66}$
Source organism	*E. coli* O157:H7	*E. coli* O157:H7	*E. coli* O157:H7
DNA source	*E. coli* O157:H7	PaaR2HisC120S	PaaR2HisC120S
Cloning *paaR2*: forward primer	AGGAGATATACCATGCAAAAAAAAGAAATTCGC (paaR2_1)	—	—
Cloning *paaR2*: reverse primer (C-His)	TCAGTGATGATGATGATGGCTGCTGCCGGCGCGGCGGCATTTTTG (paaR2_2)	—	—
Cloning *paaA2–parE2*: forward primer	GGCAGCAGCCATCATCATCATCATCACTGAGTTATAAAACCGGAGGAAAC (paaR2_3)	—	—
Cloning *paaA2–parE2*: reverse primer	GTTAGCAGCCGGATCTTAGGGAAACTGGCGTCTTG (paaR2_4)	—	—
Mutagenesis of *paaR2*: forward primer	CGGCGCAAAAAAGCCGCCGCGCT (paaR2_5)	GGCAGCAGCCATCATCATCATCATCACTGAG (paaR2_7)	GGCAGCAGCCATCATCATCATCATCACTGAG (paaR2_7)
Mutagenesis of *paaR2*: reverse primer	CAATCCATCTCGCTATGAGATCTTC (paaR2_6)	ATGATGATGGCTGCTGCCCAGATACCCTTCCGGCATCCCGTATGT (paaR2_8)	ATGATGATGGCTGCTGCCCGGTTGTTCTGCGTATTCCGCAT (paaR2_9)
Cloning vector	pET15b	pET15b	pET15b
Expression vector	pET15b	pET15b	pET15b
Expression host	*E. coli* BL21 (DE3)	*E. coli* BL21 (DE3)	*E. coli* BL21 (DE3)
Complete amino-acid sequence of the construct produced	MQKKEIRRLRLKEWFKDKTLPPKEKSYLSQLMSGRASFGEKAARRIEQTYGMPEGYLDAEYAEQPGGSPPHAGLTSNQLELLQIFSAFPEDEQRQIISELKQKKESMEDLIARWIAAQKSRRAGSSHHHHHH	MQKKEIRRLRLKEWFKDKTPPKEKSYLSQLMSGRASFGEKAARRIEQTYGMPEGYLGSSHHHHHH	MQKKEIRRLRLKEWFKDKTLPPKEKSYLSQLMSGRASFGEKAARRIEQTYGMPEGYLDAEYAEQPGSSHHHHHH

High-Fidelity 2X Master Mix (NEB). Primers PaaR2_7 and PaaR2_8 were used for the PaaR2$^{1–57}$ truncate and primers PaaR2_7 and PaaR2_9 for the PaaR2$^{1–66}$ truncate (Table 1). The final truncates contain a 3′-terminal His tag. Following PCR amplification, unmodified plasmid was degraded by incubation with DpnI for 1 h at 37°C. After confirming the deletion by sequencing, $CaCl_2$-competent *E. coli* BL21 Star (DE3) cells were transformed with the mutated plasmids. PaaR2$^{1–57}$ and PaaR2$^{1–66}$ were expressed and purified in a similar way to the full-length protein, except that a Superdex 75 16/60 SEC column (GE Healthcare) column was used in the polishing SEC step.

2.3. Generation of nanobodies

A set of ten His-tagged nanobodies were generated by the Nanobodies4Instruct centre (Steyaert laboratory, Vrije Universiteit Brussel, Brussels, Belgium) following a previously described protocol (Pardon *et al.*, 2014). In brief, the antigen (PaaR2) was injected six times into a llama along with the adjuvant GERBU LQ to stimulate the immune response. After the immune response, a sample of peripheral blood was taken containing B-cell lymphocytes. These were used to clone the affinity-matured nanobodies. cDNA was synthesized from B-cell RNA and used for nested PCR before cloning into an appropriate vector (pMESy4, GenBank KF415192), allowing release of the nanobodies in the periplasm and providing them with a C-terminal His tag (Pardon *et al.*, 2014). Panning of the potential binders to PaaR2 was performed by phage display. The vector was transformed into *E. coli* WK6Su cells for expression.

Cell cultures were grown by inoculating 10 ml preculture in 1000 ml TB medium (12 g tryptone, 24 g yeast extract, 12.55 g K_2HPO_4, 2.3 g KH_2PO_4, 0.4% glycerol in 1000 ml water pH 7.5; Tartof & Hobbs, 1987) supplemented with 100 µg ml^{-1} ampicillin, 0.1%(*w*/*v*) glucose and 2 m*M* $MgCl_2$ and shaken at 37°C and 120 rev min^{-1}. Expression of the nanobody was induced by adding 1 m*M* IPTG at an OD_{600} of 0.7. After overnight incubation at 28°C with shaking at 120 rev min^{-1}, the cells were collected by centrifugation for 10 min at 4790*g* (5000 rev min^{-1} in a JLA-8.1000 rotor). Each pellet was resuspended in 15 ml cold TES buffer [0.2 *M* Tris–HCl pH 8, 0.5 m*M* ethylenediaminetetraacetic acid (EDTA), 0.5 *M* sucrose] and left stirring for 1 h at 4°C. Next, 30 ml fourfold-diluted TES buffer was added to each suspension and further stirred at 4°C for 45 min. The periplasmic extract was obtained by centrifuging the suspension for 30 min at 4790*g* (5000 rev min^{-1} in a JLA-8.1000 rotor) and recovering the supernatant. The nanobodies were purified by IMAC using Ni^{2+}-Sepharose 6 Fast Flow medium (GE Healthcare), followed by SEC on an Enrich SEC70 column (Bio-Rad) on an ÄKTAexplorer platform (GE Healthcare). The Ni^{2+}-Sepharose medium was first equilibrated with 50 m*M* phosphate pH 7.0, 1 *M* NaCl and centrifuged for 2 min at 460*g*. The periplasmic extract was added to the medium and left to shake at room temperature for 1 h. The suspension was centrifuged for 2 min at 460*g* before loading the beads onto a PD-10 column (GE Healthcare). First, a wash step was performed using one column volume of 50 m*M* phosphate pH 7, 1 *M* NaCl solution, followed by a second wash step using two column volumes of 50 m*M* phosphate pH 6, 1 *M* NaCl. The nanobody was eluted with one column volume of 50 m*M* acetate pH 4.5, 1 *M* NaCl. Eluted fractions were neutralized in 1 *M* Tris–HCl pH 7.4 and concentrations were measured using a Nanodrop ND-1000 spectrophotometer (Thermo Fisher Scientific). Samples from the flowthrough, the two washing steps and the eluted fractions were analysed by SDS–PAGE. The fractions containing the nanobody were concentrated using Amicon Ultracel-3K filters (molecular-weight cutoff 3.5 kDa; Merck Millipore) for subsequent SEC. The column

was pre-equilibrated with phosphate-buffered saline (PBS; 137 m*M* NaCl, 2.7 m*M* KCl, 10 m*M* Na_2HPO_4, 1.8 m*M* KH_2PO_4). A 2 ml sample of nanobody in the same buffer was then injected and eluted at 1 ml min^{-1} with PBS in fractions of 0.5 ml. Fractions from the elution peak were analysed by SDS–PAGE and were stored at −20°C.

2.4. Analytical size-exclusion chromatography

Analytical SEC of the PaaR2 sample was carried out on a Shodex KW404-4F column equilibrated with 20 m*M* Tris–HCl pH 7.3, 500 m*M* NaCl. The PaaR2 sample was loaded at a concentration of 1.59 mg ml^{-1} in a volume of 0.5 ml. The PaaR2–Nb33 sample was prepared by mixing PaaR2 and Nb33 to final concentrations of 5.4 mg ml^{-1} (PaaR2) and 7.0 mg ml^{-1} (Nb33) in a final volume of 0.2 ml and running on a Bio-Rad Enrich SEC650 column. In both cases the flow rate was 1 ml min^{-1}.

Analytical SEC for the PaaR2 truncates and Nb33 samples was carried out on a Superdex Increase 75 column equilibrated with 20 m*M* Tris–HCl, 150 m*M* NaCl pH 7.5. The flow rate was 0.75 ml min^{-1}. For the analytical gel filtration of the PaaR2 truncates and Nb33 alone and together in a complex, the injection volume was 250 µl and the concentration was 1 mg ml^{-1}. The complexes of the PaaR2 truncates and Nb33 were made by mixing 2 mg PaaR2 truncate with 3.2 mg Nb33 (a 1.2-fold molar excess of Nb33) and were left to incubate at room temperature for 30 min before injection. For the analytical gel filtration of PaaR2 truncates alone at higher concentration, the injection volume was 300 µl and the concentration was 5 mg ml^{-1}. To calibrate the columns, we used the Bio-Rad Size Exclusion Standard (bovine thyroglobulin, 670 kDa; bovine γ-globulin, 158 kDa; chicken ovalbumin, 44 kDa; horse myoglobin, 17 kDa; vitamin B_{12}, 1.35 kDa). Molecular weights were estimated according to Whitaker (1963).

2.5. Mass spectrometry

Protein samples for LC-MS/MS mass spectrometry were reduced by the addition of 5 m*M* DTT, followed by incubation for 1 h at 56°C. Subsequently, a final concentration of 25 m*M* iodoacetamide was added and the samples were incubated for a further 30 min at room temperature. The proteins were then digested with mass-spectrometry-grade trypsin (Thermo Fisher Scientific) at a final concentration of 0.04 mg ml^{-1} for 18 h at 37°C. After digestion, the samples were analyzed using a Q-Exactive Orbitrap (Thermo Fischer Scientific) mass spectrometer in a shotgun analysis-type experiment following reverse-phase liquid chromatography.

For native ion-mobility mass-spectrometry experiments, samples of PaaR2 and of the nanobodies were prepared by overnight dialysis against 150 m*M* ammonium acetate buffer pH 7.3. Complexes were prepared by adding PaaR2 and nanobody together in equimolar amounts to a final concentration of 20 µ*M* each in 150 m*M* ammonium acetate buffer pH 7.3. Using in-house-prepared, gold-coated borosilicate glass needles, samples were introduced into the mass spectrometer via nano-electrospray ionization with a spray voltage of +1.6 kV. Spectra were recorded on a travelling-wave ion-mobility quadrupole time-of-flight instrument (Synapt G2 HDMS, Waters, Wilmslow, UK). Critical voltages throughout the instrument were 40 V for the sampling cone, 1 V for the extraction cone, 10 V trap collision voltage, 45 V for the trap DC bias and 0.5 V transfer collision voltage. Pressures throughout the instrument were 6 mbar, 4.3×10^{-2} mbar, 3 mbar and 3.9×10^{-2} mbar for the source, trap collision cell, ion-mobility cell and transfer collision cell, respectively.

2.6. CD spectroscopy

$PaaR2^{1–57}$ and $PaaR2^{1–66}$ were dialyzed against 10 m*M* NaH_2PO_4, 10 m*M* Na_2HPO_4, 150 m*M* NaCl pH 7.5 with two buffer changes, the second one overnight, at room temperature in Slide-A-Lyzer 3.5K Dialysis Cassettes G2 (Thermo Fischer Scientific). CD measurements were performed on a Jasco J-1500 spectropolarimeter (Jasco, Japan). Thermal denaturation was followed by measuring the ellipticity at 222 nm in the temperature range 10–95°C every 1°C with a scanning speed of 1°C min^{-1}. The CD spectra were measured between 200 and 250 nm with a scanning speed of 20 nm min^{-1} at 25°C. The signal was measured every 1 nm, with a bandwidth of 1 nm and a digital integration time of 4 s. Protein samples with a concentration of 0.3 mg ml^{-1} were measured in a quartz cuvette with a path length of 1 mm, while for samples of 0.03 mg ml^{-1} a quartz cuvette with path length 5 mm was chosen. The acquired data were normalized using the following formula to obtain the molar ellipticity $[\theta]$ in deg cm^{-2} $dmol^{-1}$,

$$[\theta] = \frac{\theta}{Ncl}, \tag{1}$$

where N is the number of amino-acid residues, c is the molar concentration and l is the path length. Melting temperatures were determined by normalizing the signal to obtain the fraction of unfolded protein (α_D) using the formula

$$\alpha_D = \frac{[\theta] - [\theta]_N}{[\theta]_D - [\theta]_N}. \tag{2}$$

$[\theta_N]$ and $[\theta_D]$ are the molar ellipticities of the native and the unfolded state determined by extrapolating the baseline before and after the transition.

2.7. Isothermal titration calorimetry

$PaaR2^{1–57}$, $PaaR2^{1–66}$ and Nb33 were dialyzed at room temperature against 10 m*M* NaH_2PO_4, 10 m*M* Na_2HPO_4, 0.01% Triton X-100, 150 m*M* NaCl pH 7.5 with two buffer changes, the second one overnight, in Slide-A-Lyzer 3.5K Dialysis Cassettes G2 (Thermo Fisher Scientific). Prior to measurements, the samples were spun down at 13 300 rev min^{-1} for 10 min and degassed on a degassing station (TA Instruments) for 30 min. The experiments were performed on a MicroCal PEAQ-ITC microcalorimeter (Malvern Panalytical) with 8.7 µ*M* Nb33 in the cell and

74.3 μ*M* PaaR2$^{1–57}$ or 80.0 μ*M* PaaR2$^{1–66}$ in the syringe. For PaaR2$^{1–66}$ data were measured at 5, 20, 32 and 37°C. For PaaR2$^{1–57}$ no usable heat signal was observed below 20°C and data were measured at 20, 25, 28 and 32°C. The heat of dilution of the PaaR2 truncates was estimated from the measured heats obtained after saturation of Nb33 and was subtracted from the titration curves. The data were analyzed with the *MicroCal PEAQ-ITC Analysis Software* using a 1:1 binding model.

2.8. Crystallization of the PaaR2–Nb33 complex

Crystallization screens were set up using (i) PaaR2 (at concentrations of 6.5, 8 and 10 mg ml^{-1}), (ii) PaaR2 with various nanobodies mixed directly into the crystallization drop at a 1:1 molar ratio (at complex concentrations of 3.5, 6 and 7 mg ml^{-1}) and (iii) a pre-purified PaaR2–Nb33 complex (at concentrations of 5.5, 6, 7, 8.2 and 11 mg ml^{-1}). The buffers used were 137 m*M* NaCl, 2.7 m*M* KCl, 10 m*M* Na_2HPO_4, 1.8 m*M* KH_2PO_4 (PBS), 20 m*M* Tris–HCl pH 7.3, 500 m*M* NaCl and 20 m*M* Tris–HCl pH 7.3, 150 m*M* NaCl. PaaR2–Nb33 complexes were prepared in a 1:1.5 ratio and concentrated to a volume of 0.5 ml using Amicon 10 kDa centrifugal filters. SEC was performed using a Bio-Rad Enrich SEC650 column which was pre-equilibrated in 20 m*M* Tris–HCl pH 7.3, 500 m*M* NaCl. The relevant fractions were pooled and the protein complex was concentrated using an Amicon Ultra 10K molecular-weight cutoff centrifugal filter.

Crystallization conditions were screened at 20 and 4°C by the hanging-drop and sitting-drop vapour-diffusion methods using Hampton Research VDX 48-well and Intelli-Plate 96-3 LVR plates or SWISSCI MRC crystallization plates. Hanging drops consisted of 1 μl protein solution (2 × 0.5 μl if PaaR2 and the nanobody were added separately) and 1 μl reservoir (or seeds in reservoir solution) and were equilibrated against 170 μl reservoir solution. Sitting drops consisted of 0.1 μl PaaR2–Nb33 solution and 0.1 μl reservoir solution and were equilibrated against 70 μl reservoir solution. Crystallization conditions were tested with several commercially available screens: Crystal Screen, Crystal Screen 2 and PEGRx (Hampton Research), ProPlex and JCSG-plus (Molecular Dimensions).

2.9. Crystallization of PaaR2$^{1–57}$ and PaaR2$^{1–66}$ in complex with Nb33

For PaaR2$^{1–57}$ and PaaR2$^{1–66}$ and their purified complexes with Nb33, crystallization conditions were screened by the sitting-drop method using Intelli-Plate 96-3 LVR plates (Hampton Research) and a Mosquito Crystallization Robot (TTP Labtech). The complexes between the PaaR2 truncates and Nb33 were prepared by mixing the proteins together in a 1:1 molar ratio. After 30 min incubation at room temperature the complexes were purified on a Bio-Rad Enrich SEC70 column. The protein concentrations used for crystallization screening ranged from 10 to 70 mg ml^{-1}. In each case, 100 nl protein solution (in 20 m*M* Tris, 150 m*M* NaCl pH 7.5) was mixed with 100 nl reservoir solution and equilibrated at 19°C against 70 μl reservoir solution from various commercial crystallization kits (Crystal Screen and Crystal Screen 2 from Hampton Research and JSCG-plus, PACT *premier* and Morpheus from Molecular Dimensions).

2.10. X-ray data collection and analysis

Crystals were flash-cooled in liquid nitrogen after transferring them to a suitable cryoprotectant solution (glycerol, PEG 400 and ethylene glycol were tried). X-ray data were measured on the PROXIMA-1 and PROXIMA-2A beamlines at the SOLEIL synchrotron facility (Gif-sur-Yvette, France) and recorded on an EIGER X 9M photon-counting area detector. Data were indexed, integrated and scaled with *XDS* (Kabsch, 2010) via the *XDSME* interface. The Laue group and space group were further verified, and potential twinning was assessed with *phenix.xtriage* (Zwart *et al.*, 2005) and *POINTLESS* (Evans, 2006). The likely unit-cell content was estimated using the *CCP*4 program *MATTHEWS_COEF* (Kantardjieff & Rupp, 2003). Data-collection statistics are summarized in Table 2.

3. Results and discussion

3.1. Production and characterization of PaaR2

Our initial construct consisted of the coding regions for the wild-type *paaR2–paaA2–parE2* operon. The presence of *paaA2–parE2* in this construct was motivated by our previous observations that the transformation of a plasmid encoding PaaR2 in the absence of PaaA2 and ParE2 is toxic to *E. coli*. The produced protein showed a tendency towards aggregation. We reasoned that this could be caused by the presence of the single cysteine at position 120. We therefore constructed the C120S mutant (De Bruyn *et al.*, 2019). PaaR2 with a hexahistidine tag at its C-terminus and including the mutation C120S was overexpressed in *E. coli* BL21 (DE3) cells and purified to homogeneity (Supplementary Fig. S1). The protein shows a single band corresponding to the correct molecular weight on SDS–PAGE. The identity of the purified protein was confirmed by LC-MS/MS mass spectrometry. The experimentally determined value of 15 295.4 ± 2.0 Da corresponds to the theoretical value of 15 296.3 Da. The yields that have been obtained in repeated purifications are between 3 and 4 mg per litre of culture medium. We previously showed that this protein forms a well folded, stable octamer and binds specifically to its operator region (De Bruyn *et al.*, 2019). Crystallization conditions were initially screened using this PaaR2 preparation, but did not lead to any crystallization hits.

3.2. Nanobodies against PaaR2

After attempts to crystallize PaaR2 on its own failed, we raised nanobodies against PaaR2 for use as crystallization chaperones. Panning of the potential binders to PaaR2 by phage display resulted in ten nanobodies with unique CDR3 sequences that could be overexpressed and purified (Fig. 1). We initially tried to preform and purify PaaR2–nanobody complexes using SEC. Addition of each nanobody to the

Table 2
Data collection and processing.

Values in parentheses are for the outer shell.

	PaaR2–Nb33	PaaR2$^{1-57}$–Nb33	PaaR2$^{1-66}$–Nb33
Diffraction source	SOLEIL	SOLEIL	SOLEIL
Beamline	PROXIMA-2A	PROXIMA-1	PROXIMA-1
Wavelength (Å)	0.980	0.979	0.979
Temperature (K)	100	100	100
Detector	EIGER X 9M	EIGER X 9M	EIGER X 9M
Crystal-to-detector distance (mm)	465.2	242.5	204.8
Rotation range per image (°)	0.1	0.1	0.1
Total rotation range (°)	360	360	360
Space group	*F*432	$P2_12_12_1$	$P3_121$ or $P3_221$
a, *b*, *c* (Å)	316.7, 316.7, 316.7	45.6, 56.6, 128.3	67.1, 67.1, 69.7
α, β, γ (°)	90.0, 90.0, 90.0	90.0, 90.0, 90.0	90.0, 90.0, 120.0
Overall *B* factor from Wilson plot (Å^2)	138.2	25.4	34.0
Mosaicity (°)	0.047	0.185	0.123
Resolution range (Å)	48.3–3.95 (48.3–11.54/4.01–3.95)†	64.1–1.60 (1.69–1.60)	44.6–1.75 (1.86–1.75)
Total No. of measured reflections	926178 (52510/142494)	564735 (69688)	371769 (55088)
No. of unique reflections	12488 (910/1936)	44565 (6812)	18776 (2991)
Completeness (%)	99.8 (100.0/99.5)	99.2 (95.1)	99.8 (99.0)
Multiplicity	74.2 (57.8/73.6)	12.7 (10.2)	7.75 (6.28)
$\langle I/\sigma(I)\rangle$	10.5 (36.6/0.89)	19.0 (1.32)	25.0 (0.85)
R_{merge}	0.462 (0.073/2.926)	0.066 (1.161)	0.054 (3.543)
R_{meas}	0.466 (0.074/2.946)	0.069 (1.221)	0.056 (3.641)
$CC_{1/2}$	0.999 (1.000/0.534)	0.999 (0.565)	0.999 (0.589)

† Because of the high overall value of R_{merge} we also provide statistics for the inner data shell to show that R_{merge} is small and compatible with the high $\langle I/\sigma(I)\rangle$, and that the high R_{merge} is not a consequence of imposing too high a symmetry. Reprocessing in lower symmetry does not significantly change the R_{merge} values.

PaaR2 solution led to visible precipitation under all conditions tried. Equally, attempts to co-crystallize PaaR2 and the different nanobodies by mixing the components directly in the crystallization drops also resulted in heavy precipitation and a failure to produce crystals.

This nanobody-induced precipitation was unexpected, and we reasoned that perhaps our nanobodies interfered with the correct oligomerization of PaaR2. When injected into the bloodstream of the llama, PaaR2 becomes diluted and the oligomeric state that is observed at higher concentrations in the test tube may partially or fully dissociate, presenting otherwise hidden surfaces to the immune system. Nanobodies interacting with such surfaces may then induce aggregation at higher protein concentrations due to incorrect oligomerization. Based on this hypothesis, we decided to screen our nanobodies for interaction with the PaaR2 oligomer using native mass spectrometry.

In agreement with our earlier work (De Bruyn *et al.*, 2019), the native mass spectrum of PaaR2 shows a single, compact charge-state distribution (Fig. 2*a*), which is characteristic of a well folded protein complex with little to no significant structural disorder (Konijnenberg *et al.*, 2013; Testa *et al.*, 2011, 2013). The corresponding mass of 122 780 Da agrees closely with the theoretical value of 122 370.4 Da for an octameric assembly of PaaR2.

The overall majority of the nanobodies displayed a rather poor binding profile in these experiments, as demonstrated by large remaining populations of free nanobody monomers and small complex populations, as shown for nanobody 14 in Fig. 2(*b*). In contrast, the mass spectrum of PaaR2 in the presence of nanobody 33 (Nb33) showed a large population of PaaR2 octamers with eight nanobodies bound (Fig. 2*c*). The spectrum of the PaaR2–Nb33 mixture contains virtually no free nanobody, suggesting that Nb33 has a high affinity for octameric PaaR2. The *m*/*z* ratio associated with the largest population in the mass spectrum indeed corresponds to a heterohexadecamer (PaaR2$_8$–Nb33$_8$) with a molecular mass of 228 kDa. We therefore decided to continue only with Nb33.

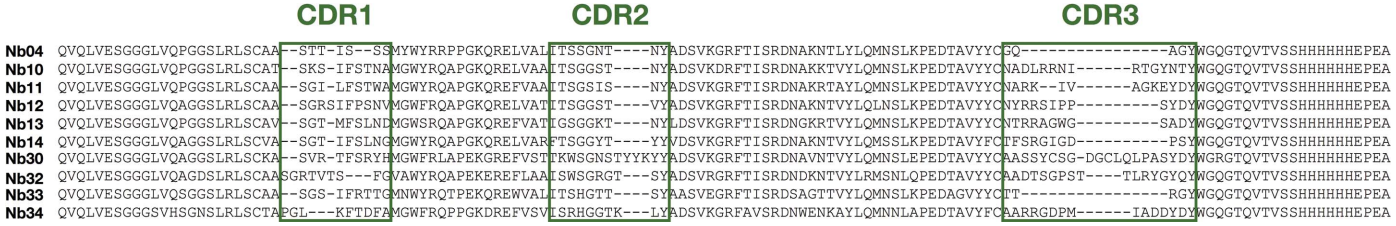

Figure 1
Nanobody sequences. A *BLAST* alignment of the ten nanobody sequences that were initially identified as binders and used in further experiments is shown. CDR regions are boxed.

3.3. Nanobody-assisted crystallization of PaaR2

Surprisingly, even Nb33 produced complexes with low solubility and precipitated at low ionic strength (150 m*M* NaCl). We therefore initially screened for crystallization conditions by mixing two separate stock solutions of PaaR2 and Nb33 in equimolar amounts directly in the drop with the precipitant solution. This strategy resulted in a hit condition when transferring the crystallization plate from 20 to 4°C, but did not result in diffracting crystals (Fig. 3*a*).

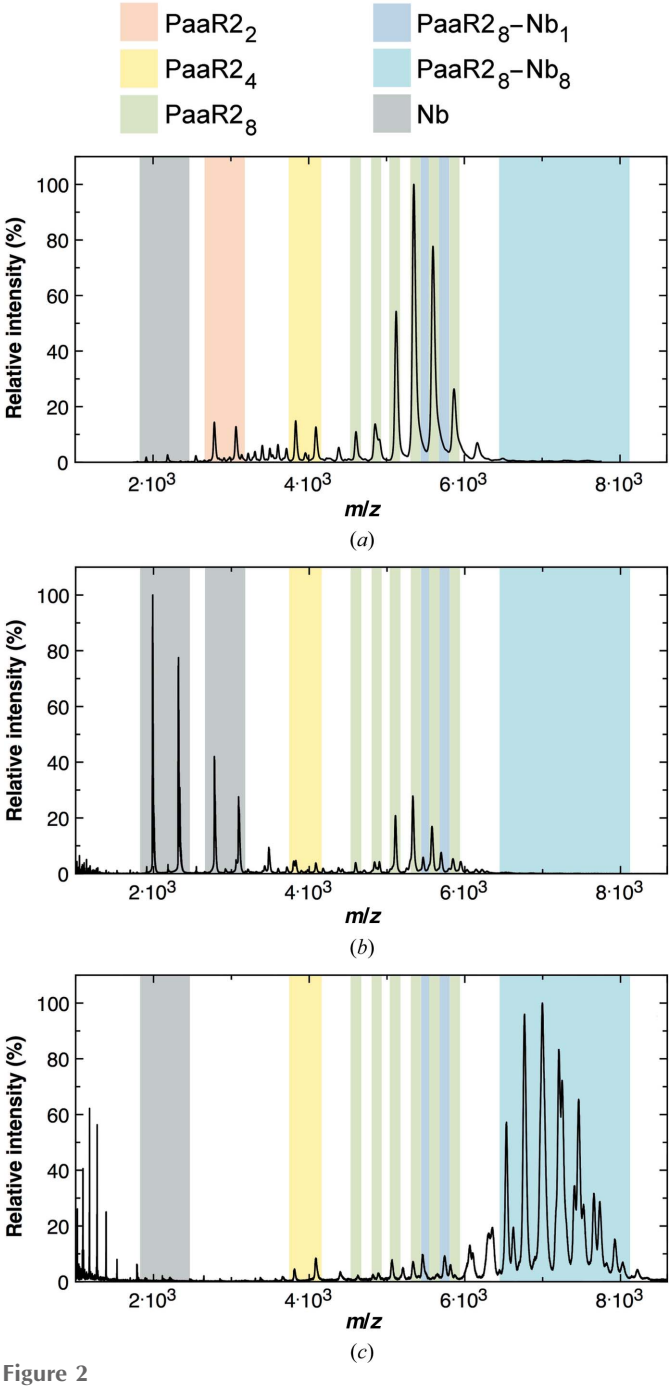

Figure 2
Native mass spectrometry. (*a*) Native mass spectrum of pure PaaR2. The spectrum mainly contains peaks corresponding to an octamer, with additional traces of a tetramer and a dimer. (*b*) In the presence of an excess of Nb14, the PaaR2 octamer remains present, and only traces of a PaaR2$_8$–Nb14 species are observed next to large amounts of free nanobody. Similar results were obtained for other nanobodies. (*c*) In the presence of Nb33, the major species becomes a PaaR2$_8$-Nb33$_8$ complex, with very little if any free nanobody or free PaaR2.

We subsequently discovered that the PaaR2–Nb33 complex is soluble at high ionic strength (500 m*M* NaCl) and room temperature, and that under such conditions the complex can be purified by SEC and concentrated to 11 mg ml^{-1} (Fig. 4*a*). This preparation was used to set up new crystallization screens, leading to a hit in 0.1 *M* sodium acetate trihydrate pH 4.6, 2.0 *M* sodium formate (Fig. 3*b*). Variation of the pH and precipitant concentration did not result in visual improvement of the crystals, but seeding ultimately led to large three-dimensional crystals in the original hit condition (Fig. 3*c*). Crystallization only occurred after incubating the complex for 2 h at 4°C, which induces precipitation that is reversible when the sample is moved to 20°C. In order to confirm the presence of both PaaR2 and Nb33, crystals were harvested, washed in artificial mother liquor and subsequently analysed by SDS–PAGE (Fig. 4*a*, inset). This analysis showed that the crystals contained both proteins in an apparently equal stoichiometry, similar to the isolated PaaR2–Nb33 complex.

Three cryoprotectants were tested using the mother liquor supplemented with 30% glycerol, 20% PEG 400 or 25% ethylene glycol. Crystals were tested on the PROXIMA-2A beamline at the SOLEIL synchrotron, Gif-Sur-Yvette, France and showed variable diffraction that was usually limited to 5–4.5 Å resolution, but always with sharp, well separated spots (Fig. 3*d*). The best diffraction was obtained from a crystal cryoprotected with 30% glycerol and provided useful data to a resolution of 4.0 Å (Fig. 3*d*). The crystals belonged to space group *F*432, with unit-cell parameter a = 317 Å (Table 2). While the $R_{\rm merge}$ and $R_{\rm meas}$ values are very high, they result from a large amount of very weak data with very high (74-fold) multiplicity. Both $R_{\rm merge}$ and $R_{\rm meas}$ increase steadily with resolution starting from reasonably low values (0.073 and 0.074, respectively) up to almost 3.00. The high-resolution cutoff was determined using $CC_{1/2}$ (Karplus & Diederichs, 2012) and $I/\sigma(I)$ dropping below 1.0, and will have to be fine-tuned during the structure-solution and refinement process. Nevertheless, we are confident that these data are valid, that the extremely high multiplicity allows the otherwise very weak data to be used to around 4 Å resolution and that the $R_{\rm merge}$ and $R_{\rm meas}$ values are therefore not informative. Matthews analysis (Matthews, 1968) suggests that the asymmetric unit is likely to contain four PaaR2 monomers and four Nb33 monomers.

3.4. Crystallization of PaaR2 truncates

In order to obtain higher resolution data, we constructed two PaaR2 truncates, PaaR2$^{1–57}$ and PaaR2$^{1–66}$, comprising the N-terminal HTH domain. Both truncates could be expressed at high levels (15 mg per litre of bacterial culture) in *E. coli* BL21, are highly soluble (can be concentrated to greater than 100 mg ml^{-1}) and behave as monomers in solution (Fig. 5*a*; Supplementary Fig. S2). The latter result indicates that the

C-terminal region, which is predicted to form a coiled-coil structure, is responsible for oligomerization. The CD spectra of the truncates indicate that they are both folded and adopt a mainly α-helical structure (Fig. 5*b*). A concentration-independent melting temperatures of 53.7°C was obtained for PaaR2$^{1–57}$. For PaaR2$^{1–66}$, the melting temperature varies with concentration: 71.2°C at 0.03 mg ml^{-1} and 73.8°C at 0.3 mg ml^{-1} (Fig. 5*c*). The latter is unexpected for a monomeric protein and suggests that PaaR2$^{1–66}$ may have a weak tendency towards oligomerization, although this was not detected in the analytical SEC experiment. The large difference in melting temperature between PaaR2$^{1–57}$ and PaaR2$^{1–66}$ further indicates that residues 58–66 significantly contribute to stability.

As for full-length PaaR2, no crystals were obtained for PaaR2$^{1–57}$ and PaaR2$^{1–66}$ alone. We therefore tested the abilities of PaaR2$^{1–57}$ and PaaR2$^{1–66}$ to bind Nb33. The analytical SEC profiles of the PaaR2 truncates mixed together with Nb33 show a peak eluting around apparent molecular weights of 15.2 and 18.5 kDa for PaaR2$^{1–57}$ and PaaR2$^{1–66}$, respectively, distinct from the elution peaks of either the truncate or the nanobody in isolation, indicating that Nb33 indeed binds PaaR2 truncates (Figs. 4*b* and 4*c*). The latter was confirmed using isothermal titration calorimetry (Fig. 6). For both PaaR2$^{1–57}$ and PaaR2$^{1–66}$ the reaction is exothermic at temperatures of 20°C or higher. Binding is endothermic at 5°C for PaaR2$^{1–66}$ but could not be measured for PaaR2$^{1–57}$. The resulting thermodynamic parameters are given in Table 3. The heat signals are very low and no reliable thermodynamic parameters could be extracted for PaaR2$^{1–57}$ at 5°C. The data were interpreted using a 1:1 binding model in each case. The derived affinities range between 0.517 and 19.1 n*M*, with the differences between PaaR2$^{1–57}$ and PaaR2$^{1–66}$ being small. However, tight binding combined with the small amounts of heat produced puts significant errors on the dissociation constants (K_d). Affinities decrease with increasing temperature. For both of the truncates the binding Gibbs energy (ΔG) is favourable and does not show significant temperature dependence due to the compensating contributions of binding enthalpy (ΔH) and entropy (ΔS). With increasing temperature the binding becomes more enthalpy-driven, while at lower temperatures it becomes more entropy-driven. The determined binding Gibbs energies at 25°C for PaaR2$^{1–57}$ and

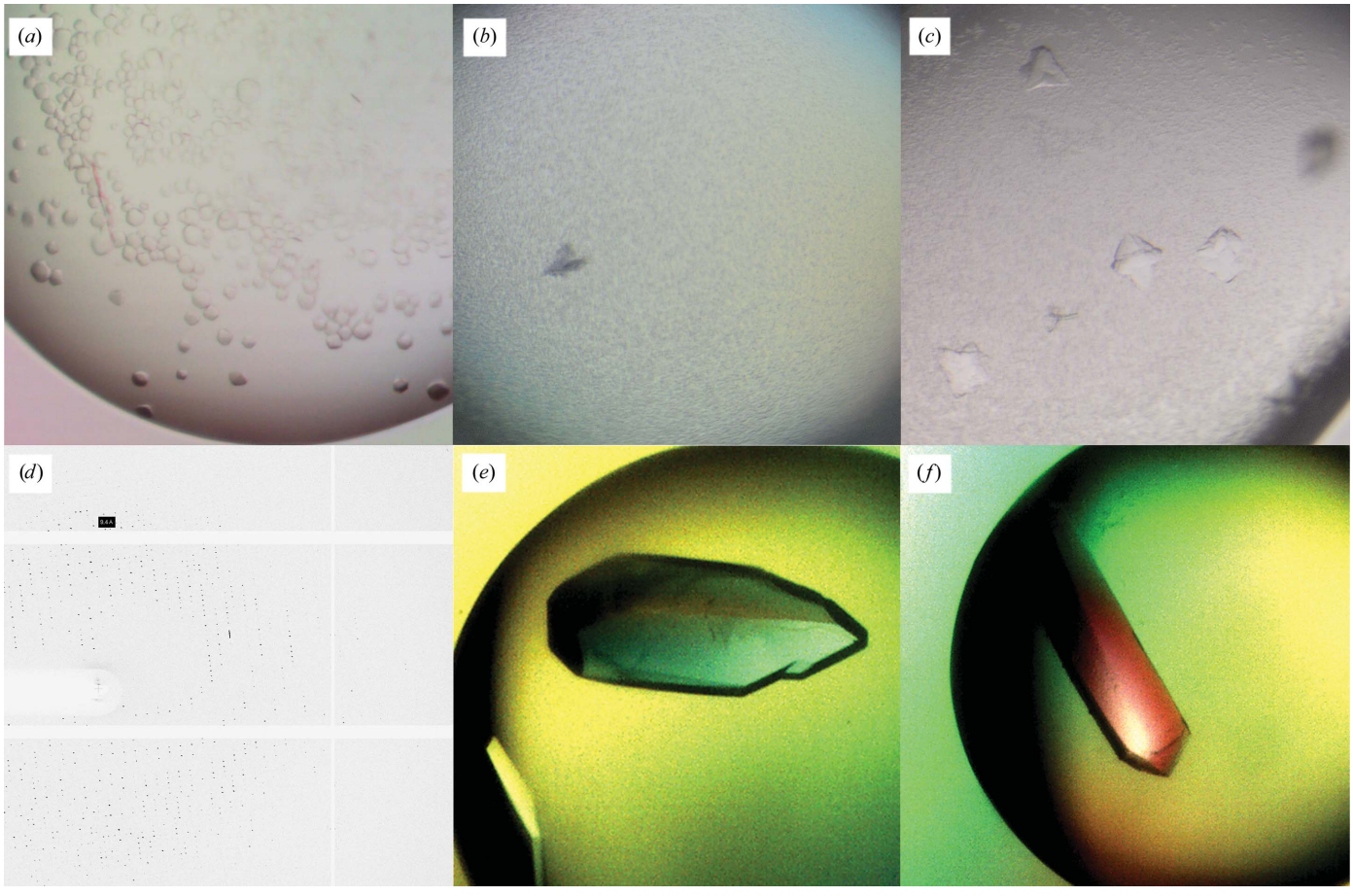

Figure 3
Crystals of the PaaR2$_8$–Nb33$_8$ complex. (*a*) Initial hit obtained by mixing PaaR2 and Nb33 in an equimolar ratio directly in the drops at low ionic strength (150 m*M* NaCl). These crystals did not show diffraction. (*b*) Shower of microcrystals obtained at 4°C using pre-purified PaaR2$_8$–Nb33$_8$ complex at high ionic strength (500 m*M* NaCl). The scale is identical to that in (*a*). (*c*) Crystals after optimization using seeding of the hit shown in (*b*). The scale is identical to that in (*a*). (*d*) Diffraction pattern obtained from a crystal similar to those shown in (*c*). (*e*) Crystal of the PaaR2$^{1–57}$–Nb33 complex used for data collection. (*f*) Crystal of the PaaR2$^{1–66}$–Nb33 complex used for data collection.

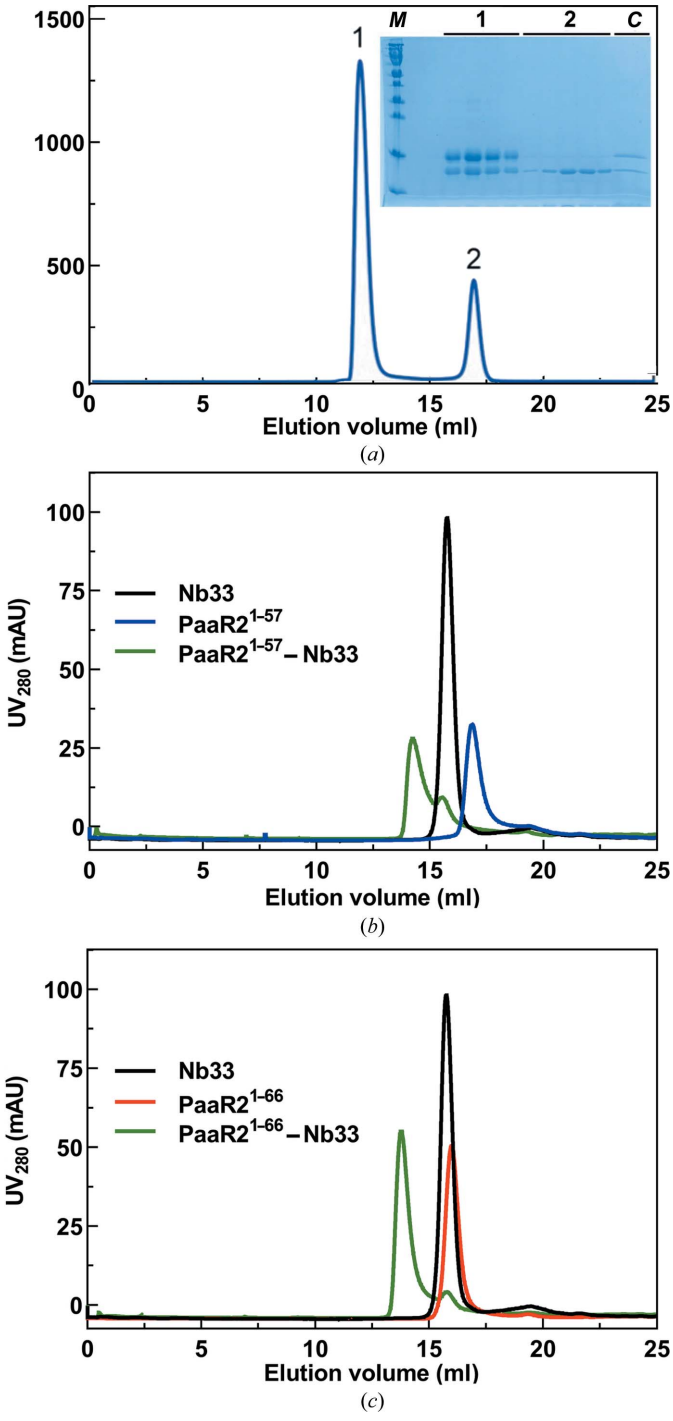

Figure 4
Preparation of the complexes with Nb33. (*a*) Analytical SEC profile of PaaR2 (5.4 mg ml^{-1} final concentration) mixed with a 1.5-fold molar excess of Nb33 (7.0 mg ml^{-1} final concentration) and injected onto a Bio-Rad Enrich SEC650 column. Peak 1 corresponds to the complex, while peak 2 corresponds to excess nanobody. The inset shows an SDS–PAGE analysis of the peaks derived from the chromatogram in (*a*). Lane *M* corresponds to the molecular-weight marker, while lane *C* corresponds to washed and dissolved crystals of the PaaR28–Nb338 complex. (*b*) Analytical SEC profiles of the PaaR2$^{1-57}$–Nb33 complex prepared using an excess of Nb33 (green) overlaid on the corresponding profiles of PaaR2$^{1-57}$ (blue) and Nb33 (black). (*b*) Analytical SEC profiles of the PaaR2$^{1-66}$–Nb33 complex prepared using an excess of Nb33 (green) overlaid on the corresponding profiles of PaaR2$^{1-57}$ (red) and Nb33 (black).

PaaR2$^{1-66}$ are −10.9 and −11.9 kcal mol^{-1}, respectively. The heat capacity change of binding (ΔC_p), determined from the linear regression of binding enthalpy versus temperature, is

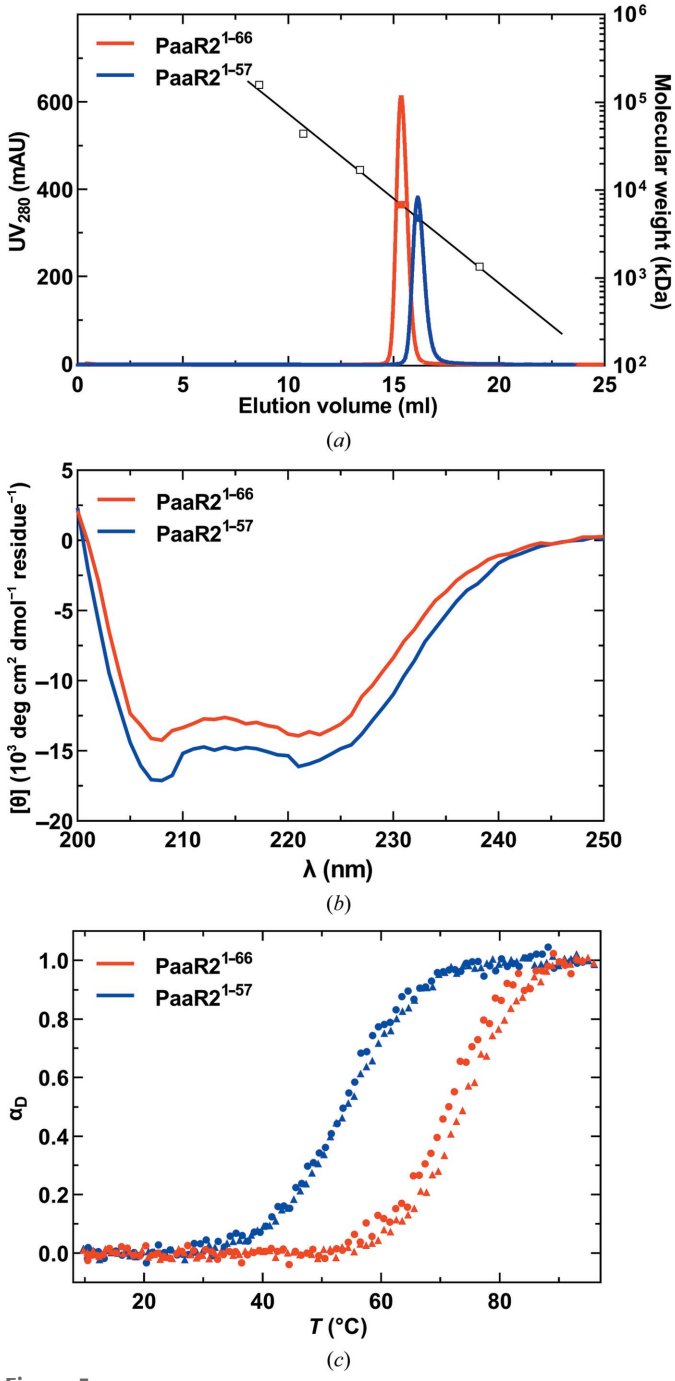

Figure 5
Biophysical characterization of PaaR2$^{1-57}$ and PaaR2$^{1-66}$. (*a*) Analytical SEC profiles of PaaR2$^{1-57}$ (blue) and PaaR2$^{1-66}$ (red) at 5 mg ml^{-1}. The elution volumes of the molecular-weight standards (bovine γ-globulin, 158 000 Da; chicken ovalbumin, 44 000 Da; horse myoglobin, 17 000 Da; vitamin B$_{12}$, 1350 Da) are plotted as white squares. The elution volumes of PaaR2$^{1-57}$ (marked as a red square) and PaaR2$^{1-66}$ (blue square) give molecular-weight estimates of 4.8 and 6.7 kDa, respectively. (*b*) CD spectra of PaaR2$^{1-57}$ (blue) and PaaR2$^{1-66}$ (red) measured at 25°C at a concentration of 0.3 mg ml^{-1}. (*c*) Thermal unfolding of PaaR2$^{1-57}$ (blue) and PaaR2$^{1-66}$ (red) followed by CD spectroscopy at 222 nm and 0.3 mg ml^{-1} (triangles) or 0.03 mg ml^{-1} (circles).

Table 3
Isothermal titration calorimetry.

Sample	Temperature (°C)	Concentration in cell (μ*M*)	Concentration in syringe (μ*M*)	*c* value	*n*	K_d (n*M*)	ΔG (kcal mol^{-1})	ΔH (kcal mol^{-1})	$-T\Delta S$ (kcal mol^{-1})	ΔC_p (cal mol^{-1} K^{-1})
PaaR2$^{1–57}$	20	8.7	74.3	4579	0.868	1.9	−11.7	−4.23	−7.48	−565
PaaR2$^{1–57}$	25	8.7	74.3	837	0.857	10.4	−10.9	−7.14	−3.75	
PaaR2$^{1–57}$	28	8.7	74.3	503	0.943	17.3	−10.7	−8.19	−2.52	
PaaR2$^{1–57}$	32	8.7	74.3	455	0.897	19.1	10.8	−11.2	0.389	
PaaR2$^{1–66}$	5	8.7	80.0	16828	0.862	0.517	−11.8	5.35	−17.2	−438
PaaR2$^{1–66}$	25	8.7	80.0	4860	0.818	1.79	−11.9	−3.98	−7.97	
PaaR2$^{1–66}$	32	8.7	80.0	861	0.880	10.1	−11.2	−6.69	−4.48	
PaaR2$^{1–66}$	37	8.7	80.0	1073	0.852	8.11	−11.5	−8.52	−2.96	

negative: −565 cal mol^{-1} K^{-1} for PaaR2$^{1–57}$ and −438 cal mol^{-1} K^{-1} for PaaR2$^{1–66}$.

Screening of crystallization conditions yielded a single condition for each complex that resulted in large, well diffracting crystals (Figs. 3*e* and 4*f*). The PaaR2$^{1–57}$–Nb33 complex crystallized at 38.48 mg ml^{-1} in 0.2 *M* sodium iodide, 20% PEG 3350, while the PaaR2$^{1–66}$–Nb33 complex crystallized at 60.42 mg ml^{-1} in 0.02 *M* sodium/potassium phosphate, 20% PEG 3350. Crystals of the PaaR2$^{1–57}$–Nb33 complex diffracted to 1.6 Å resolution and belonged to space group $P2_12_12_1$, with unit-cell parameters $a = 45.6$, $b = 56.6$, $c = 128.3$ Å. Full details of data collection are given in Table 2. Matthews analysis suggests the presence of two complexes in the asymmetric unit, with a solvent content of 37% (V_M = 1.95 Å^3 Da^{-1}).

Crystals of the PaaR2$^{1–66}$–Nb33 complex diffracted to 1.75 Å resolution and belonged to space group $P3_121$ or $P3_221$, with unit-cell parameters $a = b = 67.1$, $c = 69.7$ Å. Full details of data collection are given in Table 2. Matthews analysis indicates the presence of a single copy of the complex in the asymmetric unit, with a solvent content of 41% (V_M = 2.05 Å^3 Da^{-1}).

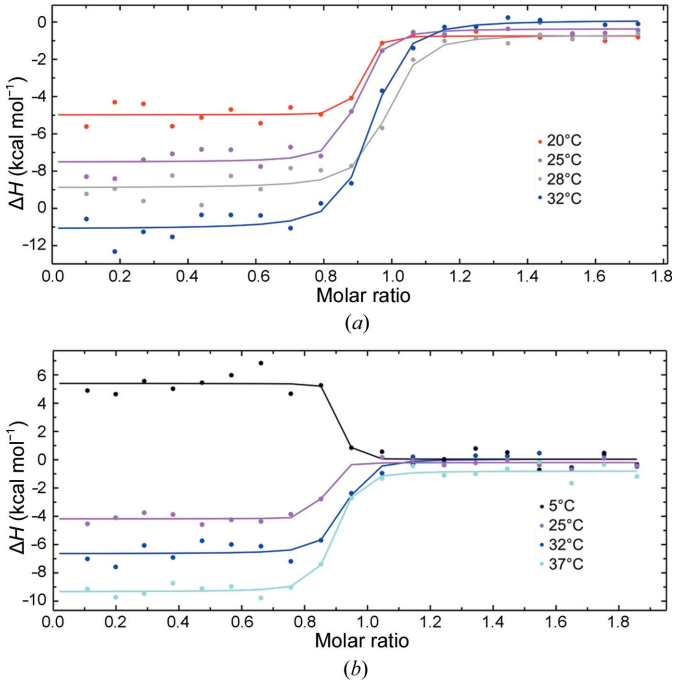

Figure 6
ITC titrations of Nb33 against PaaR2$^{1–57}$ and PaaR2$^{1–66}$. (*a*) Titrations of PaaR2$^{1–57}$ at four different temperatures. Integrated heats of binding per mole of injectant versus molar ratio ([syringe]/[cell]) for each titration step are shown. (*b*) Similar titrations for PaaR2$^{1–66}$.

4. Conclusion

We have expressed and purified the transcription regulator PaaR2 from the *E. coli* O157:H7 three-component toxin–antitoxin system *paaR2–paaA2–parE2*. Nanobodies were produced to use as crystallization chaperones for PaaR2. Via native mass spectrometry, various nanobodies were screened to find those that recognize and stabilize this oligomeric state. While most nanobodies either caused the protein solution to precipitate or resulted in too much free nanobody and PaaR2 complex, one nanobody was found that stabilized the octameric complex and forms a heterohexadecameric complex with PaaR2. This nanobody was successfully used as a crystallization chaperone for PaaR2. The same nanobody also allowed the crystallization of the monomeric N-terminal domain of PaaR2. The latter crystals diffracted to high resolution and are suitable for structure determination. The structures of PaaR2$^{1–57}$ and PaaR2$^{1–66}$ bound to Nb33 will be determined by molecular replacement using a nanobody structure stripped of the CDR loops as a search model. The structures of the resulting complexes can then be used as search models to determine the structure of full-length PaaR2 in complex with Nb33.

Acknowledgements

We thank INSTRUCT, which is part of the European Strategy Forum on Research Infrastructures (ESFRI), and the Research Foundation – Flanders (FWO) for their support during the nanobody discovery. The authors thank William Shepard for beamline support and Katleen Willibal and Sarah Haesaerts for help with the generation of nanobodies.

Funding information

This work was supported by VIB, FWO-Vlaanderen (grants G.0135.15N and G.0C12.13N, scholarship No. FWOTM637) and OZR-VUB (grant SRP13).

References

Baranova, E., Fronzes, R., Garcia-Pino, A., Van Gerven, N., Papapostolou, D., Péhau-Arnaudet, G., Pardon, E., Steyaert, J., Howorka, S. & Remaut, H. (2012). *Nature*, **487**, 119–122.

Berman, H. M., Westbrook, J., Feng, Z., Gilliland, G., Bhat, T. N., Weissig, H., Shindyalov, I. N. & Bourne, P. E. (2000). *Nucleic Acids Res.* **28**, 235–242.

De Bruyn, P., Hadži, S., Vandervelde, A., Konijnenberg, A., Prolič-Kalinšek, M., Sterckx, Y. G.-J., Sobott, F., Lah, J., Van Melderen, L. & Loris, R. (2019). *Biophys. J.* **116**, 1420–1431.

Derewenda, Z. S. & Vekilov, P. G. (2006). *Acta Cryst.* D**62**, 116–124.

Desmyter, A., Transue, T. R., Ghahroudi, M. A., Dao-Thi, M., Poortmans, F., Hamers, R., Muyldermans, S. & Wyns, L. (1996). *Nat. Struct. Mol. Biol.* **3**, 803–811.

Dumoulin, M., Conrath, K., Van Meirhaeghe, A., Meersman, F., Heremans, K., Frenken, L. G., Muyldermans, S., Wyns, L. & Matagne, A. (2002). *Protein Sci.* **11**, 500–515.

Evans, P. (2006). *Acta Cryst.* D**62**, 72–82.

Goldschmidt, L., Eisenberg, D. & Derewenda, Z. S. (2014). *Methods Mol. Biol.* **1140**, 201–209.

Hallez, R., Geeraerts, D., Sterckx, Y., Mine, N., Loris, R. & Van Melderen, L. (2010). *Mol. Microbiol.* **76**, 719–732.

Hamers-Casterman, C., Atarhouch, T., Muyldermans, S., Robinson, G., Hammers, C., Songa, E. B., Bendahman, N. & Hammers, R. (1993). *Nature*, **363**, 446–448.

Holcomb, J., Spellmon, N., Zhang, Y., Doughan, M., Li, C. & Yang, Z. (2017). *AIMS Biophys.* **4**, 557–575.

Huang, W., Manglik, A., Venkatakrishnan, A. J., Laeremans, T., Feinberg, E. N., Sanborn, A. L., Kato, H. E., Livingston, K. E., Thorsen, T. S., Kling, R. C., Granier, S., Gmeiner, P., Husbands, S. M., Traynor, J. R., Weis, W. I., Steyaert, J., Dror, R. O. & Kobilka, B. K. (2015). *Nature*, **524**, 315–321.

Hunte, C. & Michel, H. (2002). *Curr. Opin. Struct. Biol.* **12**, 503–508.

Kabsch, W. (2010). *Acta Cryst.* D**66**, 125–132.

Kantardjieff, K. A. & Rupp, B. (2003). *Protein Sci.* **12**, 1865–1871.

Karplus, P. A. & Diederichs, K. (2012). *Science*, **336**, 1030–1033.

Koide, S. (2009). *Curr. Opin. Struct. Biol.* **19**, 449–457.

Konijnenberg, A., Butterer, A. & Sobott, F. (2013). *Biochim. Biophys. Acta*, **1834**, 1239–1256.

Korotkov, K. V., Pardon, E., Steyaert, J. & Hol, W. G. J. (2009). *Structure*, **17**, 255–265.

Loris, R., Marianovsky, I., Lah, J., Laeremans, T., Engelberg-Kulka, H., Glaser, G., Muyldermans, S. & Wyns, L. (2003). *J. Biol. Chem.* **278**, 28252–28257.

Los Rios, M. de, Criscitiello, M. F. & Smider, V. V. (2015). *Curr. Opin. Struct. Biol.* **33**, 27–41.

Matthews, B. W. (1968). *J. Mol. Biol.* **33**, 491–497.

Muyldermans, S. (2001). *J. Biotechnol.* **74**, 277–302.

Pardon, E., Laeremans, T., Triest, S., Rasmussen, S. G. F., Wohlkönig, A., Ruf, A., Muyldermans, S., Hol, W. G. J., Kobilka, B. K. & Steyaert, J. (2014). *Nat. Protoc.* **9**, 674–693.

Rasmussen, S. G. F., Choi, H.-J., Fung, J. J., Pardon, E., Casarosa, P., Chae, P. S., DeVree, B. T., Rosenbaum, D. M., Thian, F. S., Kobilka, T. S., Schnapp, A., Konetzki, I., Sunahara, R. K., Gellman, S. H., Pautsch, A., Steyaert, J., Weis, W. I. & Kobilka, B. K. (2011). *Nature*, **469**, 175–180.

Rasmussen, S. G. F., DeVree, B. T., Zou, Y., Kruse, A. C., Chung, K. Y., Kobilka, T. S., Thian, F. S., Chae, P. S., Pardon, E., Calinski, D., Mathiesen, J. M., Shah, S. T. A., Lyons, J. A., Caffrey, M., Gellman, S. H., Steyaert, J., Skiniotis, G., Weis, W. I., Sunahara, R. K. & Kobilka, B. K. (2011). *Nature*, **477**, 549–555.

Roos, G., Brosens, E., Wahni, K., Desmyter, A., Spinelli, S., Wyns, L., Messens, J. & Loris, R. (2006). *Acta Cryst.* F**62**, 1255–1258.

Ruggiero, A., Smaldone, G., Squeglia, F. & Berisio, R. (2012). *Protein Pept. Lett.* **19**, 732–742.

Schubot, F. D. & Waugh, D. S. (2004). *Acta Cryst.* D**60**, 1981–1986.

Sennhauser, G. & Grütter, M. G. (2008). *Structure*, **16**, 1443–1453.

Stahl, S. J., Watts, N. R. & Wingfield, P. T. (2014). *Methods Mol. Biol.* **1131**, 549–561.

Sterckx, Y. G.-J., Jové, T., Shkumatov, A. V., Garcia-Pino, A., Geerts, L., De Kerpel, M., Lah, J., De Greve, H., Van Melderen, L. & Loris, R. (2016). *J. Mol. Biol.* **428**, 1589–1603.

Sterckx, Y. G.-J., Volkov, A. N., Vranken, W. F., Kragelj, J., Jensen, M. R., Buts, L., Garcia-Pino, A., Jové, T., Van Melderen, L., Blackledge, M., van Nuland, N. A. J. & Loris, R. (2014). *Structure*, **22**, 854–865.

Tartof, K. D. & Hobbs, C. A. (1987). *Bethesda Res. Lab. Focus*, **9**, 12–16.

Testa, L., Brocca, S. & Grandori, R. (2011). *Anal. Chem.* **83**, 6459–6463.

Testa, L., Brocca, S., Santambrogio, C., D'Urzo, A., Habchi, J., Longhi, S., Uversky, V. N. & Grandori, R. (2013). *Intrinsically Disord. Proteins*, **1**, e25068.

Tong, Y., Dong, A., Xu, X. & Wernimont, A. (2014). *Methods Mol. Biol.* **1140**, 179–188.

Uysal, S., Vásquez, V., Tereshko, V., Esaki, K., Fellouse, F. A., Sidhu, S. S., Koide, S., Perozo, E. & Kossiakoff, A. (2009). *Proc. Natl Acad. Sci. USA*, **106**, 6644–6649.

Whitaker, J. R. (1963). *Anal. Chem.* **35**, 1950–1953.

Zwart, P., Grosse-Kunstleve, R. & Adams, P. (2005). *CCP4 Newsl. Protein Crystallogr.* **43**, contribution 7.